MT9, a natural peptide from black mamba venom antagonizes the muscarinic type 2 receptor and reverses the M2R-agonist-induced relaxation in rat and human arteries

Justyna Ciolek, Claude Zoukimian, Justine Dhot, Mélanie Burban, Mathilde Triquigneaux, Benjamin Lauzier, Christelle Guimbert, Marine Ferron, Lidia Ciccone, Livia Tepshi, et al.

Biomedicine & Pharmacotherapy 150 (2022) 113094

Contents lists available at ScienceDirect

Biomedicine & Pharmacotherapy

journal homepage: www.elsevier.com/locate/biopha

MT9, a natural peptide from black mamba venom antagonizes the muscarinic type 2 receptor and reverses the M2R-agonist-induced relaxation in rat and human arteries

Justyna Ciolek [a], Claude Zoukimian [b], Justine Dhot [c], Mélanie Burban [c], Mathilde Triquigneaux [b], Benjamin Lauzier [c], Christelle Guimbert [c], Didier Boturyn [d], Marine Ferron [c], Lidia Ciccone [a,e], Livia Tepshi [a], Enrico Stura [a], Pierre Legrand [e], Philippe Robin [a], Gilles Mourier [a], Béatrice Schaack [f], Imen Fellah [c], Guillaume Blanchet [a], Chantal Gauthier-Erfanian [c], Rémy Beroud [b], Denis Servent [a], Michel De Waard [b,c,g,*,1], Nicolas Gilles [a,**,1]

[a] Université Paris Saclay, CEA, INRAE, Département Médicaments et Technologies pour la Santé (DMTS), SIMoS, 91191 Gif-sur-Yvette, France
[b] Smartox Biotechnology, 6 rue des platanes, 38120 Saint-Egrève, France
[c] Nantes Université, CNRS, INSERM, l'institut du thorax, F-44000 Nantes, France
[d] CNRS UMR 5250, Université Grenoble Alpes, Institut de Chimie Moléculaire de Grenoble, Bâtiment NANOBIO, 38041 Grenoble, France
[e] Société civile Synchrotron SOLEIL, L'orme des Merisiers Saint-Aubin - BP48, Gif-sur-Yvette, 91192, France
[f] Université Grenoble Alpes, CNRS, INP, TheRex Team, TIMC-IMAG, F-38700 La Tronche, France
[g] LabEx " Ion Channels, Science and Therapeutics ", Valbonne F-06560, France

ARTICLE INFO

Keywords:
Snake venom
M2 muscarinic receptor
Bioactive peptide mass spectrometry
Peptide sequencing, Drug screening Peptide synthesis
Peptide folding
Arterial pressure

ABSTRACT

All five muscarinic receptors have important physiological roles. The endothelial M2 and M3 subtypes regulate arterial tone through direct coupling to Gq or Gi/o proteins. Yet, we lack selective pharmacological drugs to assess the respective contribution of muscarinic receptors to a given function. We used mamba snake venoms to identify a selective M2R ligand to investigate its contribution to arterial contractions. Using a bio-guided screening binding assay, we isolated MT9 from the black mamba venom, a three-finger toxin active on the M2R subtype. After sequencing and chemical synthesis of MT9, we characterized its structure by X-ray diffraction and determined its pharmacological characteristics by binding assays, functional tests, and *ex vivo* experiments on rat and human arteries. Although MT9 belongs to the three-finger fold toxins family, it is phylogenetically apart from the previously discovered muscarinic toxins, suggesting that two groups of peptides evolved independently and in a convergent way to target muscarinic receptors. The affinity of MT9 for the M2R is 100 times stronger than that for the four other muscarinic receptors. It also antagonizes the M2R/G_i pathways in cell-based assays. MT9 acts as a non-competitive antagonist against acetylcholine or arecaine, with low nM potency, for the activation of isolated rat mesenteric arteries. These results were confirmed on human internal mammary arteries. In conclusion, MT9 is the first fully characterized M2R-specific natural toxin. It should provide a tool for further understanding of the effect of M2R in various arteries and may position itself as a new drug candidate in cardiovascular diseases

Abbreviations: ACh, Acetylcholine; Dp, *Dendroaspis polylepsis*; GPCR, G protein-coupled receptor; mAChRs, Muscarinic acetylcholine receptors; IMA, human internal mammary arteries; M2R, Muscarinic type 2 receptor; NCL, Native Chemical Ligation; [^{3}H]-NMS, [^{3}H]-N-methylscopolaline; PE, Phenylephrine; PTH, Phenylthiohydantoin; r.m.s.d., Root-mean-square deviation; TCEP, Tris (2-carboxyethyl) phosphine hydrochloride.

* Corresponding author at: Smartox Biotechnology, 6 rue des platanes, 38120 Saint-Egrève, France.
** Corresponding author.
E-mail addresses: michel.dewaard@univ-nantes.fr (M. De Waard), nicolas.gilles@cea.fr (N. Gilles).
[1] Codirected this work

https://doi.org/10.1016/j.biopha.2022.113094
Received 15 March 2022; Received in revised form 25 April 2022; Accepted 4 May 2022
Available online 10 May 2022

1. Introduction

Muscarinic acetylcholine receptors (mAChRs) are members of the G-protein-coupled receptors (GPCRs) superfamily. They contribute to multiple functions of the central and peripheral nervous systems [1], but also in vegetative processes, such as secretion of exocrine and endocrine glands, motility of the gastrointestinal tract or regulation of heart rate and cardiac output [2,3]. Distinct patterns of distributions of the five subtypes of mAChRs underlie their contributions to these important physiological functions. M1, M4 and M5 receptors are predominantly expressed in neurons and glial cells of the central nervous system, whereas the M2 and M3 receptor subtypes are also distributed in the peripheral tissues where they control the parasympathetic system. In terms of G-protein coupling, M1, M3 and M5 receptors interact favorably with G_q/11 class of α-subunit, while M2 and M4 receptors couple preferentially with $G_{i/o}$ G-proteins. In the last few years, new insights into muscarinic receptor pharmacology and structure have been described, including the resolution of M1-M4 receptors structures in both active and inactive conformations, as well as in complexes with allosteric modulators [4–7]. Thus, the molecular basis of orthosteric ligand interaction and of allosteric modulation of these receptors are now largely understood.

In the heart, acetylcholine (ACh) plays a crucial role in the control of cardiac excitability via the vagal nerve. This occurs because ACh interacts with the M2 receptor, activating its coupling to $G_{i/o}$ protein and resulting in the activation of the acetylcholine-gated inward rectifying K^+ channel [8]. Activation of this pathway is involved in reducing heart rate and slowing of impulse conduction through the atrioventricular node [9]. In coronary circulation, earlier studies using pharmacological and genetic approaches indicate that activation of both M2 and M3 receptors may mediate the ACh relaxation-mediated response [10,11]. Impairment of ACh-induced endothelial vasodilatation has been observed in several cases of cardiovascular diseases (congestive heart failure, hypertension) and may be associated with risk factors for coronary artery disease [12]. Muscarinic receptors have also been implicated in the function of mesenteric arteries, which distribute blood from the aorta to the gastrointestinal tract. Although significant levels of various muscarinic receptor mRNAs can be found in rat mesenteric arteries, the receptor subtypes being expressed remain uncertain. Hendricks et al. reported on the predominant role of the M3 receptor subtype in relaxing pre-contracted mesenteric arteries, based on their observation of high potency of M3-selective antagonists *versus* the low potencies of M1- and M2-selective antagonists [13]. Tangsucharit et al. determined that both M1 and M3 receptor subtypes, but not M2 receptor, control vasodilatation [14]. However, at the mRNA expression level, M2, M3 and M5 are all expressed in rat mesenteric arteries, while M1 and M4 receptors are undetectable [15], further complicating the picture of which muscarinic receptors are really at play in controlling mesenteric artery tone.

Due to the high homology of the orthosteric binding site among the five muscarinic receptors, the isolation or modeling of selective agonist or competitive antagonists of one specific subtype remains particularly challenging. For M2 receptors (M2R), the few molecules showing high affinity are displaying a poor selectivity factor of no more than ten-fold [16–18], thus excluding further therapeutic exploitation. Identifying more selective M2R ligands should help us in the understanding of the specific role played by this receptor subtype in several pathophysiological settings, such as cardiovascular pathologies.

Snake venoms, and mamba venoms in particular, contain a proven diversity of toxins interacting with M1 and M4 mAChRs [19,20]. These toxins of 65–66 residues belong to the three-finger fold (3FTx) structural family and display various selectivity profiles and different modes of action (antagonist or allosteric interaction) on mAChRs [21]. Some of these interactions have been investigated, for instance to unravel the molecular basis at the origin of the remarkable selectivity and allosteric property of the MT7 toxin for the M1 receptor [22,23]. Alongside, the crystallographic structure of the MT7-M1 complex was recently solved, revealing the mechanism by which this toxin regulates the receptor function [4]. Interestingly, so far only one toxin purified from the *Dendroaspis angusticeps* venom has been described as interacting with M2 receptor [24]. This M2-toxin possesses relatively low sequence identity with all other muscarinic toxins characterized so far. Unfortunately, since this peptide has been incompletely sequenced, confirmation that it interacts with high specificity with the M2 receptor, using its synthetic analog counterpart, is still lacking. However, the mere existence of such a specific toxin suggests that it should be feasible to identify a M2R-selective toxin within a snake venom.

In this manuscript, we set to identify such a M2R-selective peptide. Hence, we describe (i) the identification of a novel M2R-selective toxin using a bio-guided venom-fractionation approach, (ii) its chemical synthesis and structural crystallographic resolution, (iii) its pharmacological characterization using binding and functional experiments, and (iv) its *ex-vivo* characterization on rat and human arteries.

2. Methods

2.1. Materials

One gram of lyophilized venom of *Dendroaspis polylepis* snake (black mamba) was purchased from the African Reptiles and Venom farm (Diepsloot, South Africa). ZipTipC_{18} pipette tips were from Millipore (Merck, Molsheim, France). Trypsin, chymotrypsin, phenylephrine (PE), atropine, ACh and the mass spectrometry matrix α-cyano-4-hydroxycinnamic acid were purchased from Sigma-Aldrich (Saint-Quentin Fallavier, France). V8 protease was from Promega (Charbonnières-les-Bains, France). [^{3}H]-N-methylscopolaline ([^{3}H]-NMS) (78 Ci/mmol) was from Perkin-Elmer (Villebon sur Yvette, France).

2.2. Dendroaspis polylepis venom fractionation

The fractionation of the black mamba venom was performed as described [25]. Briefly, one weighted gram of venom was fractionated into 32 fractions on a cationic exchange liquid chromatography (50 * 400 mm column, GE Healthcare Life Sciences Europe GmbH, Buc, France). The fractions were tested at 2 μL by binding assay performed in 100 μL final. We neglected the salts contained in the venom fractions. Fraction N (31-weighted mg) was further sub-fractionated on a C_{18} Sunfire 30 * 250 mm reversed-phase column (Waters, Guyancourt, France) to generate 10 novel sub-fractions.

2.3. Determination of the primary structure of MT9

Peptide digestion and purification – 10 μg of MT9 was resuspended in 100 mM ammonium bicarbonate (pH 8), reduced 1 h at 55 °C with 17 mM Tris (2-carboxyethyl) phosphine hydrochloride (TCEP) and alkylated 1 hr with 24 mM iodoacetamide at room temperature in dark prior to enzyme digestion. The reduced/alkylated MT9 was digested by using one of the following enzymes: trypsin or chymotrypsin (for LC-ESI-QTOF MS/MS) or V8 protease (for Edman sequencing). The enzymes were added at a 1:20 ratio (enzyme/peptide, w/w) and incubated overnight at 37°C. Peptide fragments resulting from V8 protease digestion were purified using analytical RP-HPLC before Edman degradation.

Edman sequencing - The amino acid sequence determination of MT9 based on Edman degradation was performed using an Applied Biosystems gas-phase sequencer model 492. Phenylthiohydantoin (PTH) amino acid derivatives generated at each sequence cycle were identified and quantitated on-line with an Applied Biosystems Model 140C HPLC system using the data analysis system for protein sequencing from Applied Biosystems (software Procise PC v2.1). The PTH-amino acid standard kit (Perkin-Elmer, Villebon-sur-Yvette, France) was used and reconstituted according to the manufacturer's instructions. Chromatography was used to identify and quantify the derivatized amino acid

removed at each sequence cycle. Retention times and integration values of peaks were compared to the chromatographic profile obtained for a standard mixture of derivatized amino acids.

De novo MS/MS peptide sequencing - A Waters Q-TOF Xevo G2S mass spectrometer (Guyancourt, France) equipped with an Acquity UHPLC system and Lockspray source was used for the acquisition of the LC-ESI-MS and LC-ESI-MS/MS data. 10 µL of each digested peptide sample was injected into an Acquity UPLC BEH300 C_{18} column (1.7 µm, 2.1 mm ID × 150 mm L, Waters, Guyancourt, France). Peptide elution was performed at a flow rate of 0.4 mL/min with a 10–70% gradient of buffers B/A over 10 min (solvent A composition: dH_2O/formic acid, 99.9/0.1 (v/v) and solvent B composition: ACN/formic acid, 99.9/0.1 (v/v)). The eluted solution was directly injected into the coupled MS system. Acquisition and analyses of the peptide samples were carried out in the positive mode, within a mass range of *m/z* 100–2000 using the Agilent MassLynx software version 4.1 (Waters, Guyancourt, France). The mass spectrometer settings for the MS analyses were as follows: capillary voltage, 0.5 kV; cone voltage, 40 V; source temperature, 150 °C; desolvation temperature, 600°C; gas flow, 80 L/h; and gas desolvation, 1000 L/h. MS data were acquired using a data-dependent acquisition method for which MS/MS data were acquired using CID activation mode based on mass and charge state of the candidate ions. For calibration, an external lock mass was used with a separate reference spray (LockSpray) using a solution of leucine enkephalin eluted at a flow rate of 5 µL/min. The calibration was based on the MS detection of *m/z* 278.1141 and 556.2771 ions at collision energy of 23 eV. The resulting MS/MS spectra data were analyzed by De Novo sequencing using PEAKS® studio version 5.2 software (Bioinformatics Solutions Inc., Waterloo, ON, Canada) with the following settings: trypsin or chymotrypsin; carbamidomethyl (C) as a fixed modification; mass accuracy for MS/MS data at 0.05 Da; and mass accuracy for the precursor mass at 10 ppm. Amino acid sequence scores between 50 and 100 were recorded.

2.4. Determination of the disulfide bridge pattern of MT9

To define the disulfide bridge pattern of MT9, the native peptide was partially reduced with TCEP in acid conditions, alkylated a first time with a first alkylating agent, N-propylmaleimide, then each partially reduced/alkylated intermediate compounds isolated by HPLC were fully reduced and alkylated with a second alkylating agent, N-ethylmaleimide. Next, the peptide was cleaved with a variety of proteases in phosphate buffer pH 7.5 and the connectivity inferred by mass differences produced by the two alkylating agents according to LC-ESI-QTOF MS recordings.

2.5. Chemical synthesis of MT9

MT9 was synthesized by the chemical assembly of two peptide fragments (P1 and P2 from the N-terminus to the C-terminus) using hydrazide strategy for Native Chemical Ligation (NCL) [26]. The amino acid sequences of these fragments were as follows: P1 = TICHI-QISKTHGILKTCEENS-NH-NH_2 and P2 = CYKMSVRGWIIGRGCGC-PSAVRPRQVQCCTSDKCNY-OH. The two peptides were assembled stepwise using solid-phase fmoc chemistry on a Symphony Synthesizer (Protein technologies Inc.). The P1 and P2 peptides were assembled using a 2-chlorotrityl chloride resin (substitution rate of 0.4 mmol/g) functionalized with hydrazine for P1. The coupling reaction of each amino acid is taking 15 min and the reaction is repeated three times to increase the amino acid coupling yield. To further increase the yield of peptide assembly, a pseudo-proline building block was introduced in P1 at amino acid positions 7–8. After resin cleavage and deprotection with 85% (vol) trifluoroacetic acid, 5% H_2O and scavengers (1,3-dimethoxybenzene (3.75%), triisopropylsilane (2.5%) and 3,6-dioxa-1,8-octanedithiol (3.75%)), all peptides were purified to homogeneity by C_{18} RP-HPLC on a Jupiter Proteo column (4 µm, 21.2 mm ID × 250 mm L, Phenomenex, Torrance, CA, USA) using a 1260 Infinity preparative HPLC (Agilent Technologies, Les Ulis, France). After activation of P1 with $NaNO_2$, the NCL reaction was used to couple P1 and P2 in a 200 mM phosphate buffer with 6 M guanidine at pH 6.5 and the full-synthesized P1P2 peptide was purified using RP-HPLC. Molecular masses were determined by LC-ESI-QTOF MS following the syntheses of P1, P2 and P1P2 peptides. Finally, MT9 was folded/oxidized in 20% glycerol, 100 mM Tris-HCl, 1 mM reduced glutathion and 1 mM glutathione disulfide, pH 8.3 during 48 hrs. The resulting oxidized MT9 with its four disulfide bridges was purified to homogeneity using RP-HPLC. The folding states of natural and synthetic MT9 were checked by far-UV CD. The CD spectra were recorded on a Jasco 810 dichrograph using 1-mm-thick quartz cells in 300 µL of water. CD measurements were performed at 298 K, using a wavelength ranging from 260 to 190 nm. Peptide concentrations were 0.1 mM for these measurements.

2.6. Crystallization and structure determination of MT9

Crystallization experiments were carried out with lyophilized toxin dissolved at 10 mg/mL in 0.05 M sodium acetate, pH 5.5. The crystallization trials were carried out using CrystChemTM sitting drop vapor diffusion plates with 1 µL drops of protein and 1 µL drops of precipitant, stored in a constant temperature incubator at 20 °C. Limited screening for crystals was carried out following the protocol used for AncTx1-W28R/I38S [27]. Crystals of MT9 were obtained from 1.05 M ammonium sulfate, 0.06 M sodium citrate, pH 5.5 with 35 mM NaSCN as an additive. Twelve crystals were flash frozen in a cryo-loop with a cryoprotectant consisting of 80% saturated lithium sulfate, a general purpose cryo-salt for crystals obtained at high ionic strength [28]. Five of these gave usable X-ray diffraction data at the synchrotron Soleil (St. Aubin, France) on beamline Proxima-2A [29]. The XDS6 [30] was used for data reduction by xdsme script [31]. The crystals belonging to the orthorhombic space-group C222 with cell parameters a = 69.5, b = 93.6, c = 62.2 Å diffracted between 2.3 and 1.9 Å resolution. The structure was solved by molecular replacement starting from the crystal structure of atratoxin-b, a short-chain α-neurotoxin from *Naja atra* venom (PDB ID: 1ONJ) [32] with Phaser [33]. Refinement was carried out with REFMAC [34], Phenix [35] and BUSTER and the electron density fitted with COOT [36]. Data collection and refinement statistics for the MT9 structure are reported in Table 1. The RMSD analysis was carried out

Table 1
Statistics for MT9 crystallographic structure: data collection, processing and refinement.

PDB code	6R5M
Data Collection	
Synchrotron source	Soleil Proxima-2A
Wavelength (Å)	0.980097
Space group	C222
Cell parameters (Å)	69.5 93.6 62.2
Molecules/asymmetric unit	3
Resolution (Å)	47–1.9 (2.01–1.9)
Rmeas (%)	19.9 (140)
Rfact (%)	17.3 (105.7)
Mean I/σ (I)	6.6 (1.4)
CC1/2 (%)	99 (67.1)
Completeness (%)	99.7 (98.6)
Multiplicity	6.0 (6.0)
Refinement	
Resolution (Å)	47–1.9 (2.01–1.9)
Number of reflections	16,290 (1164)
R*work*[a](%)	22.0 (30.0)
Rfree[a] (%)	25.1 (35.6)
r.m.s.d. deviation[a]	
Bond lengths (Å)	0.010
Bond angles (°)	1.23
Ramachandran	
Favored (%)	97.58
Outliners (%)	0

[a] Data were from BUSTER output.

using LSQKAB and SUPERPOSE. The figures have been made with PyMOL [37] and CHIMERA. The electrostatic potential map was calculated using PDB2PQR web server [38].

2.7. Phylogenetic analyses

The sequence dataset from Blanchet et al. [39] containing all the known 3FTx from the four mamba species was used (*Dendroaspis intermedius* was not yet distinguished from *Dendroaspis angusticeps* at the time of the different toxin description). Sequences were named according to their SwissProt accession number and the species name. MT9 was incorporated into the dataset and the sequences were realigned using MUSCLE implemented in MEGA6 [40]. A mild gap opening value (−4) was used to prevent the alignment to be too scattered or compacted. The alignment was then used to estimate the best model of evolution (in complete depletion mode). The best estimated model of evolution (WAG model using a discrete gamma distribution (+G) and with invariance on certain sites (+I-)) was set accordingly in the option parameters of the Maximum Likelihood (mL) method.

2.8. Pharmacological characterization

All binding experiments were performed as described [41] and adapted to the 96-well plate format. Plates were filtered on a harvester and counted on a TopCount machine (Perkin-Elmer, Villebon sur Yvette, France). The human M2 receptors were stably expressed in the Chinese Hamster Ovary (CHO) cell line as described previously [41]. Briefly, 0.8–3 nM of [^{3}H]-NMS was incubated between 2 and 3 hrs with a mix of M2R membranes and variable concentrations of competitors at 22 °C in a PBS-BSA buffer (10 mM sodium phosphate, pH 7.2, 135 mM NaCl, 2.5 mM KCl, 0.1% BSA). Analyses were performed with KaleidaGraph software (Synergy Software, Reading, PA, USA) using a non-linear Hill equation. K_i values were calculated by the Cheng and Prusoff equation ($Ki = IC_{50}/ 1 + [L^*/K_d]$, where L* is the concentration of the hot ligand and K_d is its dissociation constant [42].

All cAMP quantifications were performed with the homogeneous time-resolved fluorescence-based cAMP Dynamic II assay kit (Cisbio, Codolet, France) according to the manufacturer's instructions. M2R-expressing CHO cells were detached and suspended in HAM/F12 medium at a cell density of 500 cells/μL and 5 μL of this suspension were used for each assay point in 384 small volume well plates (Greiner Bio-One, Les Ulis, France). Five μL of ligand solutions (twofold concentrated), prepared in 50 mM HEPES pH 7.5 and 50 μM forskolin, were then added to each well and the plates were incubated for 30 min at 37 °C. cAMP detection reagents, supplemented with 1 mM 3-isobutyl-1-methylxanthine to avoid cAMP degradation, were added and the plates incubated for 1 h at room temperature before fluorescence measurement in a ClarioStar plate reader (BMG Labtech, Champigny-sur-Marne, France). Results were expressed as ratios of fluorescence intensities measured at 665 and 620 nm (after excitation at 320 nm) x 10,000.

2.9. Vascular reactivity of isolated arteries

Rats were housed under standard conditions of temperature (21–24 °C), humidity (40–60%) and 12 h light/dark cycle. All animal experimental protocols were approved by the Pays de la Loire Ethical Committee and were performed in accordance with the French law on animal welfare, EU Directive 2010/63/EU for animal experiments, the National Institutes of Health Guide for the Care and Use of Laboratory Animals (National Institutes of Health Pub. No. 85–23, revised 2011). Second-order rat mesenteric arterial rings were mounted on a multi-channel isometric myograph (Model 610M, Danish Myo Technology, Denmark) at 37 °C in a physiological salt solution (Krebs-Henseleit) with the following composition (in mM): 119 NaCl, 4.7 KCl, 25 $NaHCO_3$, 1.17 $MgSO_4/7$ H_2O, 2.5 $CaCl_2$, 1.18 KH_2PO_4 and 11 glucose, continuously bubbled with 95% O_2 and 5% CO_2. Two tungsten wires (25 μm in diameter) were inserted into the lumen of the arteries and respectively fixed to a force transducer and a micrometer. Mesenteric arterial rings were stretched at wall tension corresponding to a pressure of 90 mm Hg. After an equilibration period (at least 20 min) under this optimal passive tension, arteries viability and maximal contractile capacity of the vessels were tested by two successive contractions in response to 80 mM KCl depolarization and 10 μM PE. Endothelial function was assessed by the ability of ACh to induce relaxation (80–100% of pre-contracted vessels). After a 20-min washout period mesenteric arterial rings with functional endothelium were pre-contracted with 10 μM PE and then exposed to increasing incremental concentrations of ACh (0.1 nM to 100 μM) to study endothelium-dependent relaxation. Schild regression built with cumulative concentration-responses to ACh or arecaine were performed in the presence of synthetic MT9 or atropine after 30 min incubation. Each data point represents the average of between n = 2–4 arterial rings per preparation and 5 preparations were used before averaging the results.

A similar investigation was carried out on human internal mammary arteries (IMA) from patients undergoing coronary artery bypass surgery. The research was carried out in accordance with the Declaration of Helsinki of the World Medical Association. The biocollection was approved by an independent ethics committee in France (Comité de Protection des Personnes OUEST IV). Informed consent was obtained from every individual participant included in the biocollection. The artery segment collected during the operation was directly placed in a Tyrode solution (in mM: NaCl 130, KCl 5.6, $MgCl_2$ 1, $CaCl_2$ 2, Glucose 11, HEPES 8, pH = 7.4) and the sample directly transferred to the laboratory within 4 hrs. As described for rat mesenteric arteries, the vessels were dissected and mounted on stainless steel wires in a 3 mL organ bath containing Krebs solution maintained at 37 °C and oxygenated with a 95% O_2, 5% CO_2 gas mixture. Isometric tension was recorded by a transducer (IT2, EMKA Technologies, Paris, France) and data were recorded and analyzed using IOX software (EMKA Technologies, Paris, France). After 30 min of equilibration IMA were stretched at wall tension of 2.5 g, the viability of IMA was challenged twice with 90 mM KCl and the integrity of endothelial function was checked by the induction of 50% relaxation with ACh after pre-contraction with 1 μM PE. For this study IMA rings were contracted with 1 μM PE and a cumulative concentration-response curve to arecaidine (1 nM to 100 μM) was performed in presence of MT9 at 1 μM.

2.10. Statistical analyses

All values are expressed as mean ± SEM for n experiments (n representing the number of animals). Relaxations to the different drugs were expressed as percentage relative to the PE-induced precontraction. Comparison of vascular reactivity parameters was performed using general linear mixed model with Gaussian distribution and assessed graphically. Statistical analysis was performed using a two-way analysis of variance test followed by Bonferroni's post-hoc test as appropriate using GraphPad Prism software (version 5.04; GraphPad Software Inc., CA, USA). $p < 0.05$ was considered to be statistically significant.

3. Results

3.1. Identification of MT9 from dendroaspis polylepis venom

Binding of [^{3}H]-NMS was performed on CHO cell membranes stably expressing the M2R. The venom of *Dendroaspis polylepsis* (Dp) was fractionated by cation exchange chromatography (Fig. 1A). The fraction N, that significantly inhibited [^{3}H]-NMS binding, is shown on the chromatogram (Fig. 1A). Sub-fractionation of fraction N provided ten daughter fractions (Fig. 1B), among which fraction E was detected as active and which is shown on the chromatogram (Fig. 1B). LC-ESI QTOF MS analysis revealed the presence of a single product of $[M+H^+]^{4+}$ = 1588.99, corresponding to a calculated monoisotopic mass of 6351.9

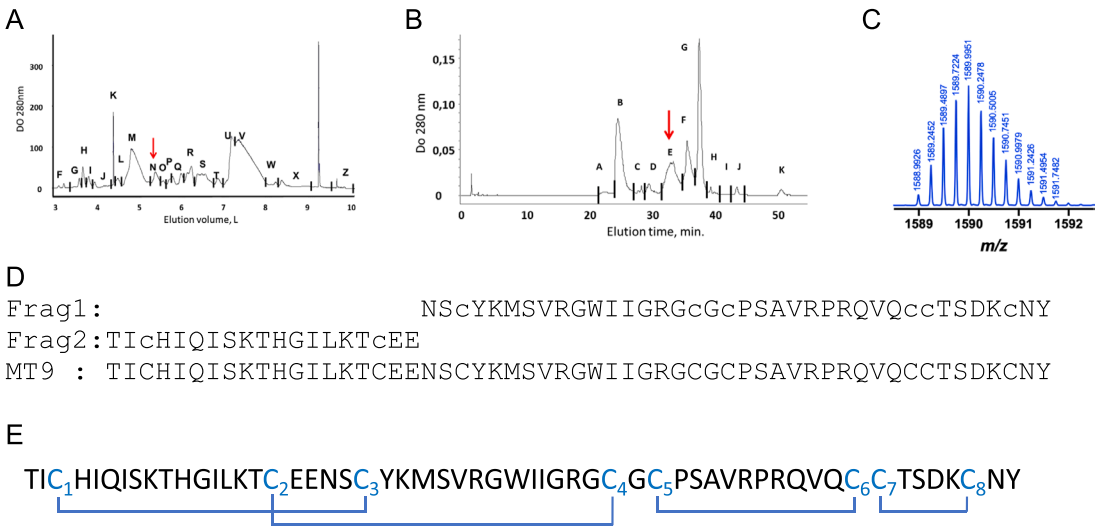

Fig. 1. Discovery, identification and synthesis of the MT9 peptide. (A) Fractionation of 1 g of *Dendroaspis polylepis* venom on a cationic exchange liquid chromatography. (B) Fractionation of the fraction N (31 mg) on a reversed phase liquid chromatography. The red arrow indicates the active pics, inducing at least 50% of [^{3}H]-NMS binding inhibition. (C) Mass measurement of MT9 by LC-ESI QTOF showing a $[M+H^+]^{4+}$ of 1588.99. (D) MT9 peptide sequences determined by Edman sequencing of the two fragments resulting from V8 protease digestion of reduced/alkylated MT9 (Frag1 and Frag2). c: iodoacetamide-modified Cys residue. The total sequence of MT9 is shown as a result. (E) Disulfide pairing of MT9 as determined experimentally.

(Fig. 1C). We named this new toxin MT9, the 9th-discovered muscarinic toxin, because the latest published muscarinic toxin is MT7 [43] while MT8 is still under investigation. The reduced/alkylated E sub-fraction has a molecular weight of 6816.8 Da indicating the presence of 8 cysteine residues in MT9 (Fig. S1). Proteolytic digestion of this reduced/alkylated MT9 with the V8 protease provides two peptide fragments of 4567.1 and 2267.1 Da (Fig. S1). The molecular weights of these two fragments (minus 18 Da for the peptide link) added up to the full-length reduced/alkylated peptide. Both peptide fragments were next characterized by Edman sequencing (Fig. 1D). The presence of a Glu residue at the C-terminus of the smallest molecular weight peptide is coherent with the cleavage site by protease V8 and indicates that it represents the N-terminal fragment of MT9. The advantage of Edman sequencing is that it allows for the identification of Leu *versus* Ile residues, hard to distinguish by MS/MS techniques. To confirm these data, the reduced/alkylated MT9 was also digested by trypsin or chymotrypsin, and the resulting peptide fragments directly analyzed by LC-ESI-QTOF MS/MS. Trypsin and chymotrypsin digestions lead to 12 and 6 fragments, respectively, covering 100% of the peptide (Fig. S1). De novo sequencing was performed for all detected *m/z* ions and the retrieved sequences perfectly matched the ones detected by Edman sequencing. This is exemplified in two representative examples of MS/MS spectra that illustrate *de novo* sequencing of MT9, one after trypsin digestion of reduced/alkylated MT9 and the other after chymotrypsin digestion (Fig. S1). All peptides were identified with error inferior to 6.4 parts per million. The full sequence of the peptide present in the E sub-fraction was construed from all these data (Fig. 1D).

Because MT9 contains four disulfide bridges, which creates an impressive number of disulfide bridging combinations, we set to determine the disulfide bridge organization of the native MT9 peptide. To that end, we used a partial MT9 reduction procedure along alkylation of the free cysteine residues with a first alkylating agent, N-propylmaleimide, and a complete reduction, alkylation with a second alkylating agent, N-ethylmaleimide. Using this procedure, combined to protease digestion, we managed to infer the disulfide bridging pattern of MT9 by LC-ESI-QTOF MS. From these recordings, the disulfide bridge arrangement was shown to be C1-C3, C2-C4, C5-C6 and C7-C8 (Fig. 1E). All subsequent experiments were performed with the synthetic form of the MT9.

3.2. Chemical synthesis and structural characterization of MT9

MT9 was chemically synthesized using solid-phase Fmoc chemistry and NCL. Two peptide fragments, P1 and P2 (TICHIQISKTHGILKT CEENS-NH-NH_2, 2368.20 Da and CYKMSVRGWIIGRGCGCPSAVRPRQ VQCCTSDKCNY-OH, 4023.84 Da), were chemically synthesized and purified to homogeneity (Fig. 2A,B). P1 and P2 were ligated to each other to produce reduced MT9 (theoretical molecular weight of 6360.00 Da) with a yield of 39%. Next, the MT9 peptide was folded/oxidized in conditions that yielded 45% of correctly folded peptide (Fig. 2C). Oxidized/folded MT9 is more hydrophobic than reduced MT9 since it elutes with later in the elution conditions on RP-HPLC. The synthetic peptide coeluted perfectly with the natural MT9, indicating that the folding of the peptide occurred properly (Fig. 2D).

Crystals of MT9 were obtained using the previously described AncTx1-W28R/I38S protocol for a three-finger fold toxin [27]. The crystallographic structure of MT9 was solved by molecular replacement using a short-chain α-neurotoxin from *Naja atra* venom (PDB ID: 1ONJ) [32]. The crystals were grown into orthorhombic space group C222 with cell parameters a = 69.67, b = 93.84 and c = 62.3 Å diffracted at 1.9 Å resolution (Table 1). With one molecule of MT9 in the asymmetric unit, the superposition of molecule A with its symmetric B and C showed a slight shift of side-chain orientation of Trp^{30} and Arg^{28} at the tip of loop II and the Arg^{43} in loop III (Fig. 3A). Nevertheless, the range of root-mean-square deviation (r.m.s.d.) on Cα of all MT9 residues between 0.22 and 0.60 Å suggested good superposition of the three monomers. We found that MT9 is a three-finger fold peptide with a very short loop 2. Interestingly, the superposition of MT9 (PDB ID: 6RM5) with fasciculin-2 (PDB ID: 1FCS), an anti-cholinesterase toxin, shows a good overlap in loops II and III of these toxins, even if the fingers II and III of fasciculin-2 are longer by 3 and 1 residues. Major structural differences are visible at the tip of loop I (Fig. 3B). The r.m.s.d. on Cα between the two crystallographic structures is 6.58 Å. The comparison of MT9 with the curare-mimetic erabutoxin b (PDB ID: 6EBX) shows a perfect superposition of loop III, while the overlap in loop II is only partial, due to important difference in length (Fig. 3C). In addition, slight differences at the extremity of loop I between the two toxins were observed. The r.m.s.d. Cα value between MT9 and erabutoxin b is 9.37 Å. Strikingly, comparison between the two MT9 and MT7 (PDB ID: 2VLW) muscarinic toxins highlights that relevant structural differences exist in their three

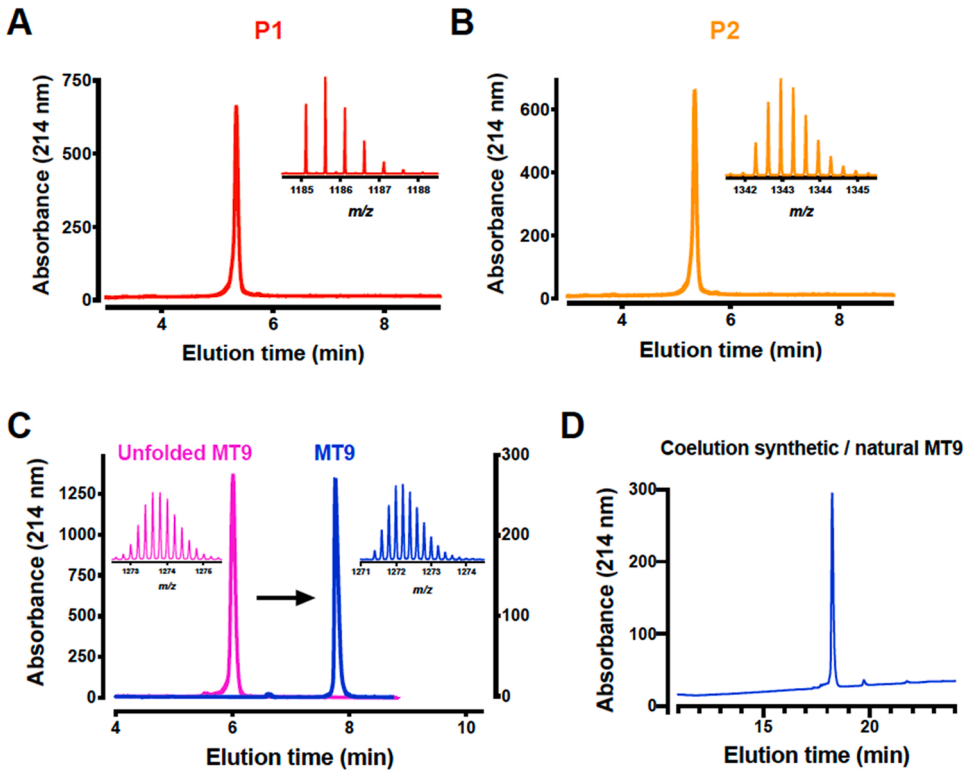

Fig. 2. Chemical synthesis of MT9. (A) Chemical synthesis of P1 fragment of MT9. LC-ESI QTOF MS in inset. (B) Chemical synthesis of P2 fragment of MT9. Inset: LC-ESI QTOF MS. (C) Elution profiles of the reduced MT9 peptide after NCL of P1 and P2, and of the folded/oxidized MT9. Insets: LC-ESI QTOF MS profiles of both peptides indicating proper folding and oxidation. (D) Coelution of natural and synthetic MT9 showing perfect identity of the peptides.

loops in agreement with the larger r.m.s.d. value on Cα: 9.72 Å. Indeed, important variations in the length of loop II and in the orientation of the tip of loops I and III are observed (Fig. 3D).

The electrostatic surface potential representations of MT9, fasciculin-2, erabutoxin b and MT7 were calculated using PDB2PQR web server [38]. They highlight differences in charge distribution between these separate 3FTx (Fig. 4). MT9 and fasciculin-2 displayed similar distributions of charged residues, in agreement with their respective pI values of 9 and 8.7. The main difference was observed at the apex of the concave face of their loops III, where positive and negative residues appeared in MT9 and fasciculin-2, respectively. As compared to MT9, the pI of erabutoxin b (8.2) and MT7 (7.7) were significantly less basic, in agreement with larger electronegative surfaces located on the two toxin's faces and more particularly at the top of their structures and in their loops II and III (Fig. 4).

3.3. Phylogenetic analysis of MT9

A blast analysis reveals that closest sequences to MT9 also come from mamba venoms. Yet, they possess different pharmacological properties (Fig. 5A). C13S1C1 with 53% of identity displays a cytotoxic activity against non-small cell lung adenocarcinoma A549 cells [44,45]. Calciseptin (49% identity) blocks the L-type calcium channel [46], while Fasciculin-2 (51% identity) is an acetylcholinesterase blocker [47]. Finally, 42% of sequence identity was observed with erabutoxin b, a short-chain nicotinic toxin (Fig. 5A). Among all known muscarinic toxins, MT9 shared the highest sequence identity (44%) with the partially characterized M2-toxin [24]. This percentage decreased to 28–31% with toxins known to interact selectively with M3 and/or M1 subtypes of mAChRs (Fig. 5A). The relationship between MT9 and the other mamba 3FTxs was also evaluated by molecular phylogeny as shown in Fig. 5B. In this tree of mamba 3FTx, all the previously described functional or orphan groups (as in [48] and [39]) were present with excellent statistical supports. MT9 appeared to be a sister sequence of the M2-toxin, yet with a low statistical support and relatively long branches. Both the MT9 and the M2-toxin belong to a subgroup that contains the fasciculins, the calciseptin- and mambin-type toxins, as well as the type I alpha-neurotoxins and the orphan groups X and XI. This MT9-subgroup differs from all other functional toxin groups (aminergic toxins, mambalgins and type II alpha-neurotoxins) with significant statistical evidence.

3.4. Pharmacological characterization of synthetic MT9

The ability of synthetic MT9 to inhibit [^{3}H]-NMS binding on each of the five muscarinic receptor subtypes was first evaluated. MT9 specifically binds the M2R subtype since it inhibits [^{3}H]-NMS binding with an IC_{50} value of 0.79 μM (calculated K_i of 120 nM), while the peptide had no effect on the four other muscarinic receptor subtypes at concentrations up to 100 μM (Fig. 6A). Conversely, however, NMS itself inhibits [^{3}H]-NMS binding with an IC_{50} of 3.6 nM. As illustrated, the average MT9 inhibition curve shows some flatness compared to that of NMS with its Hill slope of 0.98. In reality, Hill slopes for MT9 inhibition were found to fluctuate between 0.65 and 1.0 (average of individual values: 0.88 ± 0.2, n = 6), while the Hill slopes for [^{3}H]-NMS binding were between 0.8 and 1.1 (average of 0.98 ± 0.15, n = 8). These slopes were independent of the incubation time (2–4 h tested) or the [^{3}H]-NMS concentration used (between 0.8 and 3 nM). Therefore, we infer that this shallow slope should arise from the averaging process and the differences between NMS and MT9 kinetic properties. It was thus not further investigated.

M2R is preferentially coupled to the G_i protein and its activation leads to adenylyl cyclase inhibition and hence to a decrease in intracellular cAMP concentration. The pharmacological effect of MT9 was determined on CHO cells stably expressing the M2R. Forskolin dose-dependently induces up to 60 nM of cAMP production in M2R-

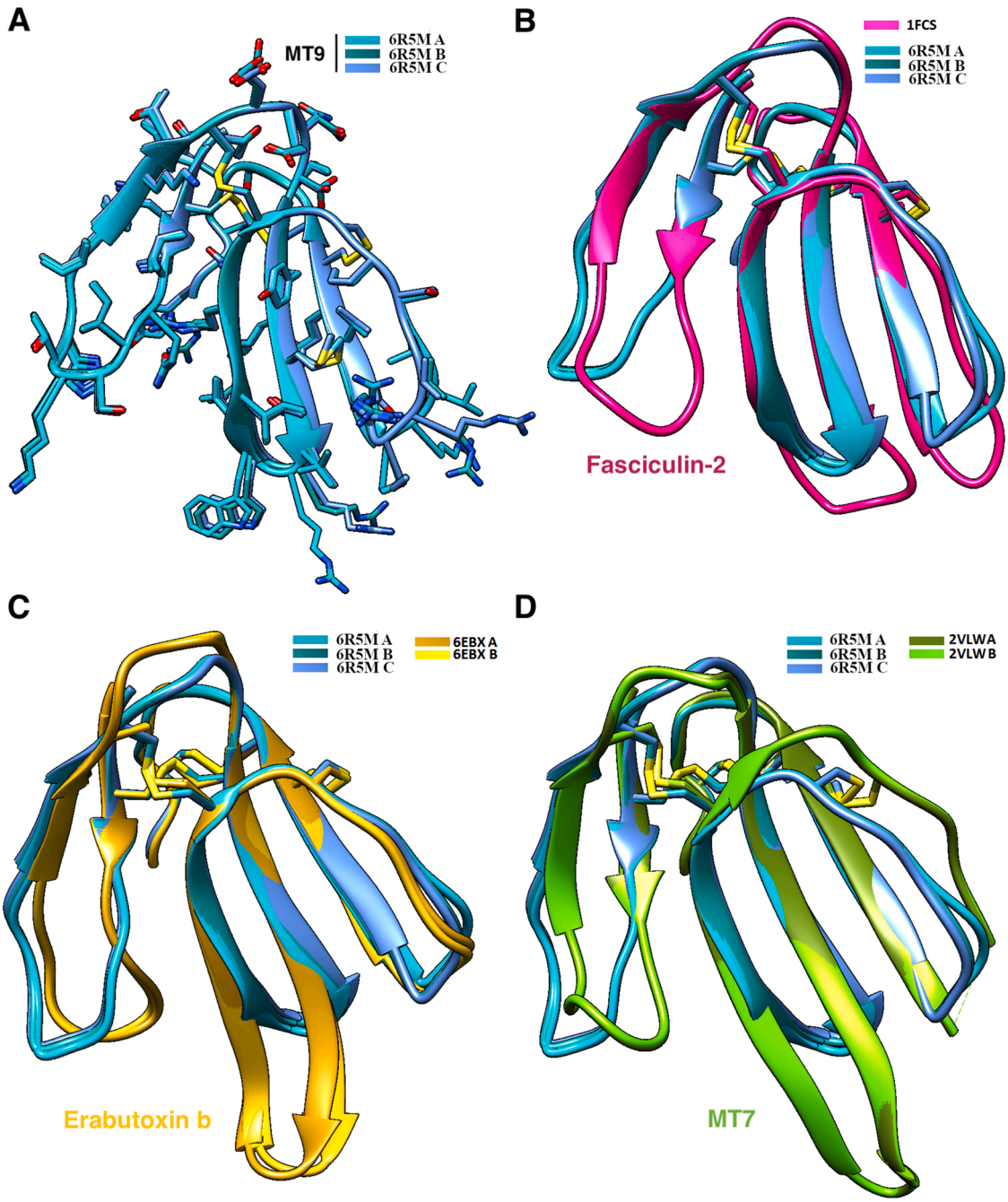

Fig. 3. Structural characterization of MT9. (A) Superposition of the three MT9 molecules in the asymmetric unit (cyan monomer A, sea green monomer B, sky blue monomer). (B) Superposition of MT9 (cyan) with fasciculin-2 (deep pink). (C) Superposition of MT9 (cyan) with the short neurotoxin erabutoxin b (goldenrod monomer A and gold monomer B). (D) Superposition of MT9 with the MT7 muscarinic toxin (monomer A light green and monomer B deep green).

expressing CHO cells with an EC_{50} of 21 μM (data not shown). In the presence of 25 μM forskolin, CHO cells produced 50 nM of cAMP. Under that condition, up to 100 μM of MT9 never reduces cAMP production demonstrating that this peptide lacks agonist activity on M2R (Fig. 6B). In contrast, under identical experimental conditions, carbachol, an M2R agonist, inhibits cAMP production in a dose-dependent manner with an IC_{50} value of 3.5 nM. In the presence of 25 μM forskolin, supplemented with a maximally effective concentration of carbachol (100 nM), both NMS and MT9 restore cAMP production with EC_{50} values of 0.7 nM and 9.5 μM, respectively (Fig. 6C). This confirms the potent antagonist activity of NMS on carbachol effects. It also demonstrates for the first time the antagonist property of MT9 on carbachol effects on M2R in the presence of forskolin. Assuming a competitive behavior of MT9 in this system, we calculated the approximate MT9 K_D using the formula $K_D = [MT9]/(shift - 1)$ with $[MT9] = 11$ μM and $shift = 100/3.5$. Under our conditions, MT9 $K_D = 399$ nM, a value coherent with the K_i obtained by binding studies (120 nM).

3.5. *Ex vivo functional evaluation of MT9*

The vascular resistance of mesenteric arteries is highly adaptable and these arteries therefore represent a good model to study contractibility. Also, since the identity of muscarinic receptors controlling the tone of arteries is disputed, this study represents a good opportunity to assess the effects of MT9 (Fig. 7). Rat mesenteric arterial rings were mounted on a multichannel isometric myograph and connected to a force

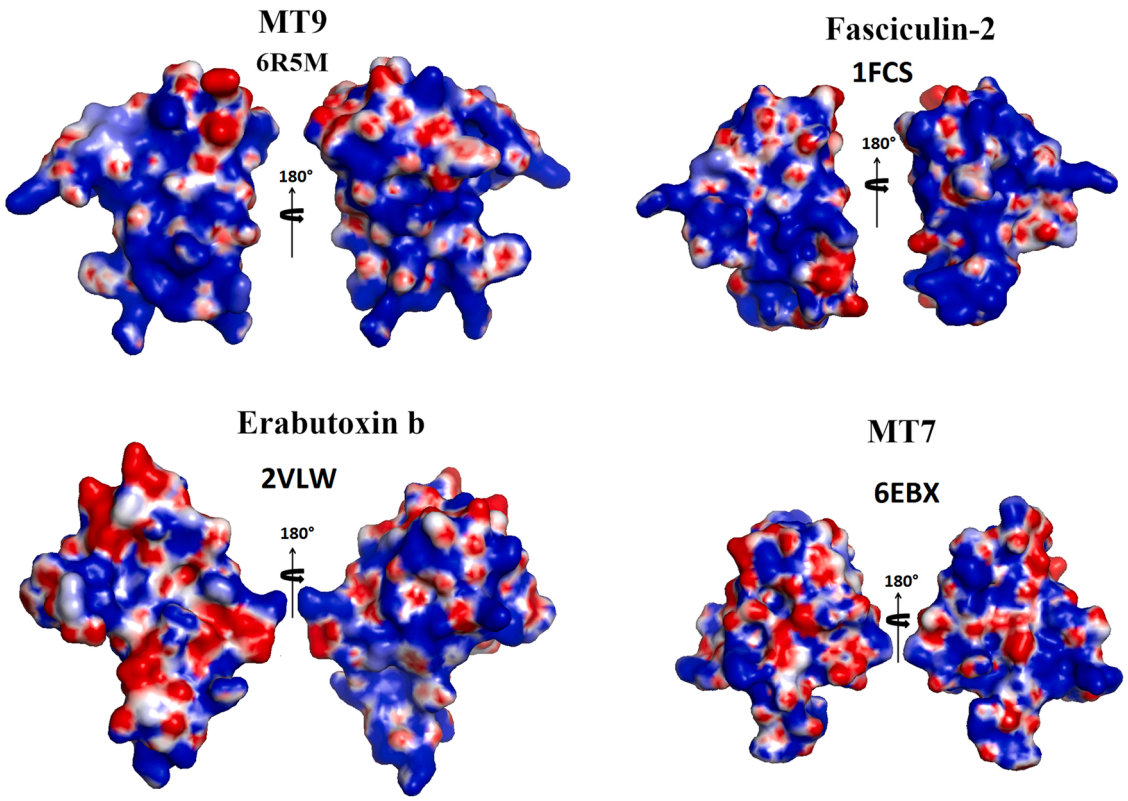

Fig. 4. Comparisons of electrostatic potential maps of MT9 with other 3FTx. Electrostatic potential maps calculated using PDB2PQR web server [38] of MT9 (PDB ID: 6R5M, upper left), fasciculin-2 (PDB ID: 1FCS, upper right), Erabutoxin- b (PDB ID: 2VLW, lower left) and muscarinic toxin MT7 (PDB ID: 6EBX, lower right). Red and blue design acidic and basic residues, respectively.

transducer and a micrometer. After stretching mesenteric arterial rings at 90 mm-Hg wall tension and exerting additional pre-contraction with 10 μM phenylephrine (PE), the endothelial function was assessed by incremental increases of ACh concentration to induce relaxation (between 80% and 100% of pre-contracted vessels). ACh induced artery relaxation with an IC_{50} of 29.1 nM ($LogIC_{50}$: −7.536 ± 0.085, Fig. 7 A). In the presence of increasing concentrations of atropine, a high affinity non-selective muscarinic antagonist, preincubated 30 min before ACh application, the concentration-response curve to ACh shifted to the right with ever increasing IC_{50} values (i.e., 128 nM at 1 nM atropine and 10.1 μM at 1 μM atropine) (Fig. 7A, Table 2). Since rat mesenteric arteries have a high receptor reserve and that ACh-induced relaxation can occur with a low level of receptor occupancy, it is logic that low concentrations of atropine, a competitive antagonist, induces a parallel rightward shift in the ACh concentration-curve. Interestingly, at the highest concentrations of atropine, that will logically impact the high receptor reserve of the preparation, we witness a depression of the maximal response of relaxation of ACh. These effects are attributed mainly to the lack of equilibration due to the slow dissociation of atropine from the receptor.

We also established dose-response curves for arecaidine on inducing artery relaxation since this compound as a M1R and M2R agonist [49]. In the absence of any other compound, arecaidine produces full artery relaxation with an IC_{50} of 89.7 nM ($LogIC_{50}$: −7.047 ± 0.1218) (Fig. 7B). Similarly to ACh, the concentration-response curve to arecaidine also shifted to the right in the presence of atropine (i.e., IC_{50} of 127.3 nM at 1 nM atropine up to 2.57 μM at 1 μM atropine) (Fig. 7B, Table 2). Here also, a depression of the maximal response of relaxation in response of arecaidine is observed at the highest concentrations of atropine that impacts the high receptor reserve of the preparation.

Next, we studied the effect of MT9 on ACh-induced relaxation since MT9 acts as a carbachol antagonist. Increasing concentrations of MT9 was also found to steadily shift the concentration-response curve to ACh to the right (Fig. 7C). Surprisingly, and contrary to expectations based on [^{3}H]-NMS binding and cAMP production data (Fig. 6), MT9 started to be effective at nanomolar concentration on ACh-induced relaxation. Indeed, the IC_{50} for ACh-induced relaxation shifted to 73.7 nM ($LogIC_{50}$: −7.132 ± 0.1437) in the presence of 0.8 nM of the toxin (Table 2). At higher MT9 concentrations, the observed IC_{50} values for ACh-induced artery relaxation shifted further to the right (i.e., 129 nM at 8 nM MT9 and 1.55 μM at 8 μM MT9) (Fig. 7C, Table 2). As for ACh, increasing concentrations of MT9 also shifted the concentration-response curve to arecaine to the right (i.e., IC_{50} values for arecaine-induced artery relaxation from 184.5 nM at 0.8 nM MT9 to 1.27 μM at 8 μM MT9) (Fig. 7D, Table 2). The antagonistic effect of 80 nM of MT9 seemed much more powerful when the arteries were relaxed by arecaine than by ACh. Indeed, 80 nM of MT9 only shifted the ACh IC_{50} value by 10.7-fold, while it shifted the arecaine one by 26.5-fold.

We also used Schild representations to illustrate these findings. When using ACh as a relaxant, the atropine Schild slope of 0.793 ± 0.034 appeared to be significantly higher than the MT9 one, of 0.42 ± 0.05. The pA_2 extracted was equal to 9.56 ± 0.41 for atropine and to 8.95 ± 0.25 for MT9 (Fig. 7E). Also, if arecaidine is used as a relaxant, rather than ACh, a Schild representation illustrates again a lower slope (0.364 ± 0.082) for MT9 compared to 0.672 ± 0.063 for atropine. The Schild pA_2 extracted was 9.43 and the Schild pA_2 for atropine was 8.67 (Fig. 7 F). For both, Fig. 7E,F, with Schild plot slopes significantly different from 1, the pA_2 value does not represent an estimate of the K_d value of MT9.

We noticed that there is a clear interruption in the progressive shift of the ACh concentration response curve at MT9 concentrations of 80 and 800 nM (Fig. 7 C). This can also be seen if arecaidine is used instead of ACh (Fig. 7D). It is also partially visible on the Schild plot if a smooth curve through the data had to be plotted. Besides this observation, the

A

```
MT9        TICHIQISKTHGILKTCE--ENSCYKMSVRG---WII---GRGCG--CPSAVRPRQVQ-CCTS-DKCNY   100
C13S1C1    RICYSHKLLQAKTTKTCE--ENSCYKRSLPKIPLIII---GRGCG--CPLTLPFLRIK-CCTS-DKCN-    53
Acetyl-C   TICYSHTTTSRAILKDCG--ENSCYRKSRRHPPKMVL---GRGCG--CPPGDDYLEVK-CCTSPDKCNY    53
Fas2       TMCYSHTTTSRAILTNCG--ENSCYRKSRRHPPKMVL---GRGCG--CPPGDDNLEVK-CCTSPDKCNY    51
C10S2C2    RICYSHKASLPRATKTCV--ENSCYKMFIRTSPDYIS---DRGCG--CPTAMWPYQTA-CCKG-DRCNK    49
Calcisep   RICYIHKASLPRATKTCV--ENTCYKMFIRTQREYIS---ERGCG--CPTAMWPYQTE-CCKG-DRCNK    49
S4C8       RICYTHKSLQAKTTKSCE--GNTCYKMFIRTSREYIS---ERGCG--CPTAMWPYQTE-CCKG-DRCNK    49
m2-tox     RICHSQMSSQPPTTTFCR--VNSCYRRTLRDPHDPRGTIIVRGCG--CPRMKPGTKLE              44
Eb         RICFNHQSSQPQTTKTCSPGESSCYNKQWSDFRGTII---ERGCG--CPTVKPGIKLS-CCES-EVCNN    42
MT7        LTCVKSNSIWFPTSEDCPDGQNLCFKRWQYISPRMYDF--TRGCAATCPKAEY-RDVINCCGT-DKCNK    31
MT1        LTCVTSKSIFGITTENCPDGQNLCFKKWYYIVPRYSDI--TWGCAATCPKPTNVRETIRCCET-DKCNE    28
MT3        LTCVTKNTIFGITTENCPAGQNLCFKRWHYVIPRYTEI--TRGCAATCPIPEN-YDSIHCCKT-DKCNE    28
Tx24       LTCVKSNSIRFPTSGDCPDGQNLCFKRWQSPGMPRPMW--ALVCAATCPKAPP-NEDINCCGT-DKCNK    26
```

B

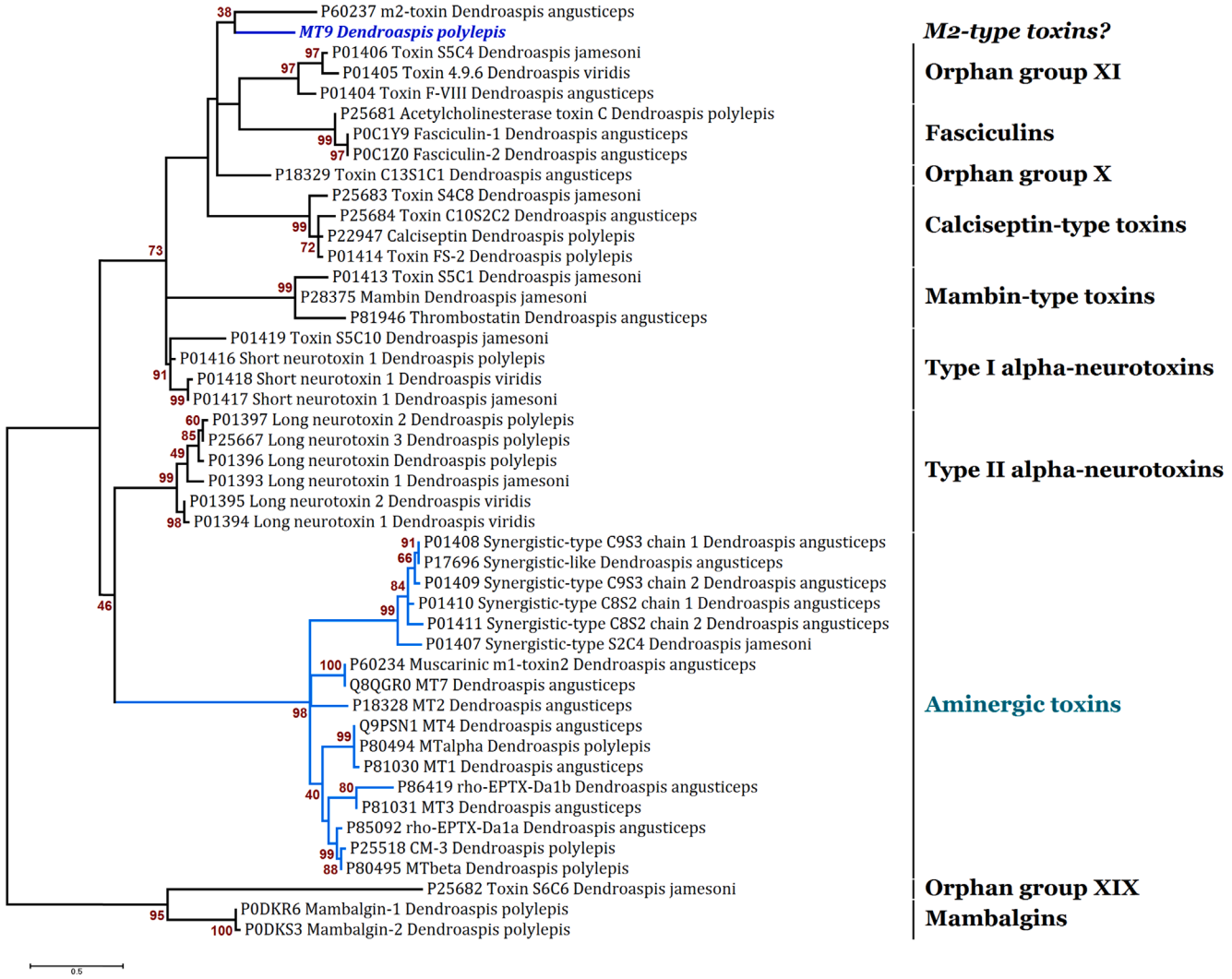

Fig. 5. Phylogeny analysis of MT9. (A) MT9 sequence compared to sequences of 3FTX representative of the anti-cholinesterase (Fasciculin-2 (Fas2)), nicotinic (erabutoxin b (Eb)) and muscarinic toxins (MT9). Cysteines are highlighted in gray. Bold residues are those that differ from MT9 sequence. The number at the end of each peptide sequence represents the percentage of identity with MT9. (B) Maximum likelihood tree of MT9 and the 3FTx identified in mamba venoms. The tree was manually edited in MEGA6 with the toxin groups name based on Fry's nomenclature [48]. Bootstrap values based on 1000 replicates with values below 35% were omitted. Blue lines show active toxins on aminergic GPCRs.

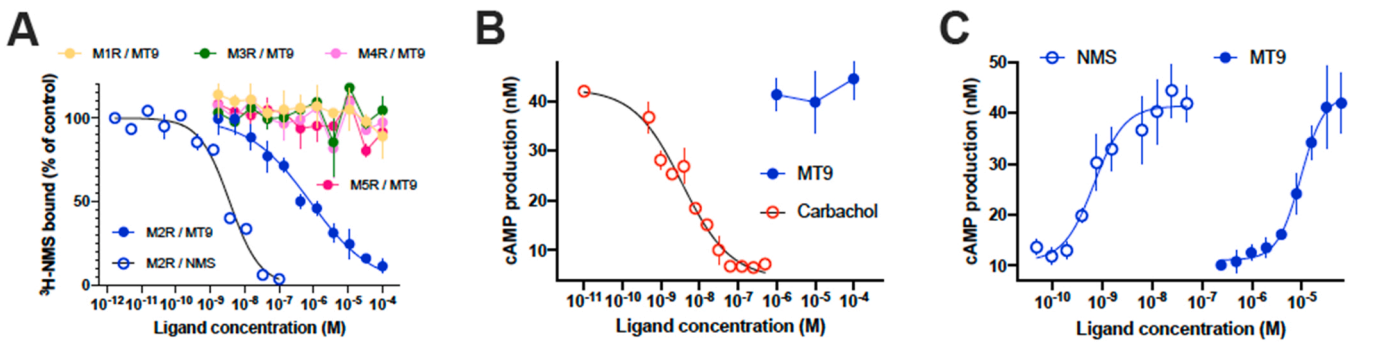

Fig. 6. Pharmacological characterization of MT9. (A) Inhibition of [^{3}H]-NMS binding on the five human muscarinic receptor subtypes by NMS (open blue symbol on M2R only) or MT9 (full colored symbols on all muscarinic receptors). [^{3}H]-NMS Hill slope on average data (0.99, n = 8); MT9 Hill slope on average data (0.48, n = 6). (B) Inhibitory effect of carbachol (red symbol) and absence of effect of MT9 (full blue symbol) on the production of cAMP induced by forskolin on CHO cells expressing M2R. (C) Antagonistic activities of NMS (open blue symbol) and MT9 (full blue symbol) on the inhibitory effect of 100 nM carbachol on forskolin-induced cAMP production. Replicate between 3 and 8. Data are mean values ± SEM (n = 5–8).

inhibition of function seems also more potent than inhibition of binding. The interpretation of this effect is not easy but several possibilities can be mentioned. A combination of high potency allosteric inhibition and a lower potency direct competitive inhibition cannot be excluded and may be supported by the expected large interaction surface such a peptide may have with M2R. Alternatively, the mechanism of inhibition of rat mesenteric relaxation by some MT9 concentrations used herein may involve a process different than inhibition of muscarinic receptor. These data hint to the fact that it will be interesting to assess the binding of MT9 on a set of GPCRs larger than the muscarinic ones.

We also tested the antagonistic effect of MT9 on human internal mammary arteries rings. In an earlier study investigating the competitive antagonism of selective M1R, M1/M3R and M2R antagonists, the authors concluded about the predominant expression of M1R, without excluding a contribution of M2R and M3R [50]. On this human preparation, the arecaidine response was biphasic. Arecaidine relaxed arteries with an EC_{50} of 3.8 nM ($LogEC_{50}$: −8.413 ± 1.441) for the high affinity component and with an EC_{50} of 11.7 μM ($LogEC_{50}$: −4.931 ± 0.5439) for the second phase. In the presence of 1 μM of MT9, the high affinity arecaidine EC_{50} shifted to 29.24 nM ($LogEC_{50}$: −7.534 ± 0.1085), while the low affinity one hardly changed with an EC_{50} of 15.2 μM ($LogEC_{50}$: −4.819 ± 0.1473). MT9 specifically antagonized the high-affinity arecaidine binding sites on the mammary arterial rings (shift of the EC_{50} of more than 7 times) but had no effect on the low-affinity arecaidine binding site, confirming the presence of at least two types of muscarinic receptors in this preparation.

4. Discussion

Three-finger fold toxins represents one of the most common structural fold in Elapidae snake venoms. The functional plasticity of this fold supports pleiotropic functions by interacting with a large diversity of molecular targets including ion channels (ASIC, Ca_v, KcsA), receptors (nAChRs, mAChRs, $GABA_A$-R), enzymes (PLA2, AChE) or cell membranes [51]. Nevertheless, by blocking the activity of the nicotinic and muscarinic acetylcholine receptors or by inhibiting the acetylcholinesterase, three-finger fold toxins interfere more particularly with the cholinergic function [52] and this property was discovered and described more than 50 years ago [53,54]. More recently, several three-finger fold toxins were isolated from Dendroaspis snake venoms and characterized for their property to interact with GPCRs (muscarinic, adrenergic, dopaminergic) [55]. Interestingly, even if these toxins often interact with their respective targets with high affinity and selectivity, they are not associated with a toxic effect and their presence in the mamba venoms is still not fully understood.

MT9 identified in this manuscript is a new example of such pharmacological property with more than a hundred-fold in selectivity for the M2R compared to the four other muscarinic receptors. The phylogenetic reconstruction surprisingly showed that this novel toxin is not part of the historical aminergic toxin group toxins formally described [39], which include all the 3FTx known to interact with mAChRs and those associated with synergistic property. It is therefore obvious that an aminergic function evolved independently (also termed convergence) in the mamba venoms with MT9, and for a second time on the 3FTx scaffold. In our analysis, MT9 was associated with the M2-toxin, previously characterized with a weak inhibition on M2 subtype. The presence of MT9 in our alignment disrupted M2-toxin from grouping with the neurotoxins and introduced the possibility of a second radiation of aminergic/muscarinic 3FTx from the mamba venoms. However, the low statistical evidence, due to a well-known difficulty in properly aligning highly divergent short sequences with numerous gaps and the fact that the pharmacological activity of the M2-toxin has never been confirmed, prevented us to confirm such hypothesis. Further *in silico* analysis using only the super group (regrouping the fasciculins, the calciseptin- and mambin-type toxins, the type I alpha-neurotoxins and the orphan groups X and XI) did not help at precisely retracing the relationship of MT9 and M2-toxin (data not shown). In the case that MT9 and M2-toxin are unrelated, and the activity of m2-toxin confirmed, it may imply that an aminergic function has evolved not only 2, but 3 times on a 3FTx scaffold by convergence in the mamba venoms, and a M2 function twice. This is unique, especially when considering the yet to be tested functional effect of aminergic toxin in mamba's preys or predators. Our discovery also brings one more evolutionary wonder. None of the classical muscarinic toxins was ever shown to interact with the M2 subtype, yet we now have found that precise function in a distantly related 3FTx, MT9. The absence of M2 activity in the aminergic toxin radiation is baffling. Hypothetically, if MT9 evolution predates the apparition of the aminergic toxin radiation, it may have constrained a later evolution of M2 activity. We do hope that future discovery of intermediary sequences will improve our understanding of the molecular evolution of the mamba 3FTx and the functional convergence of the venom aminergic function.

In agreement with the "atypical" location of MT9 on the evolutionary tree, MT9 also possesses unique structural characteristics in this functional aminergic family, mainly located in its central loop II. Indeed, MT9 loop's II is the shortest in size (only 13 residues instead of 17), lacks highly conserved residues of muscarinic toxins (Pro^{33}-Arg^{34}) and displays a unique exposed Trp^{30} at the top of this loop. These unique characteristics, associated with the highly critical role of the 3FTx loop's II in the receptor recognition, may suggest an original mode of interaction of this toxin of M2R. The presence of a specific positively charged cluster in the MT9 loop III, associated with the presence of two unusual Arg residues in 3FTx (Arg^{43} and Arg^{45}) that could specifically interact with the negatively charged EDGE sequence, located in the extracellular

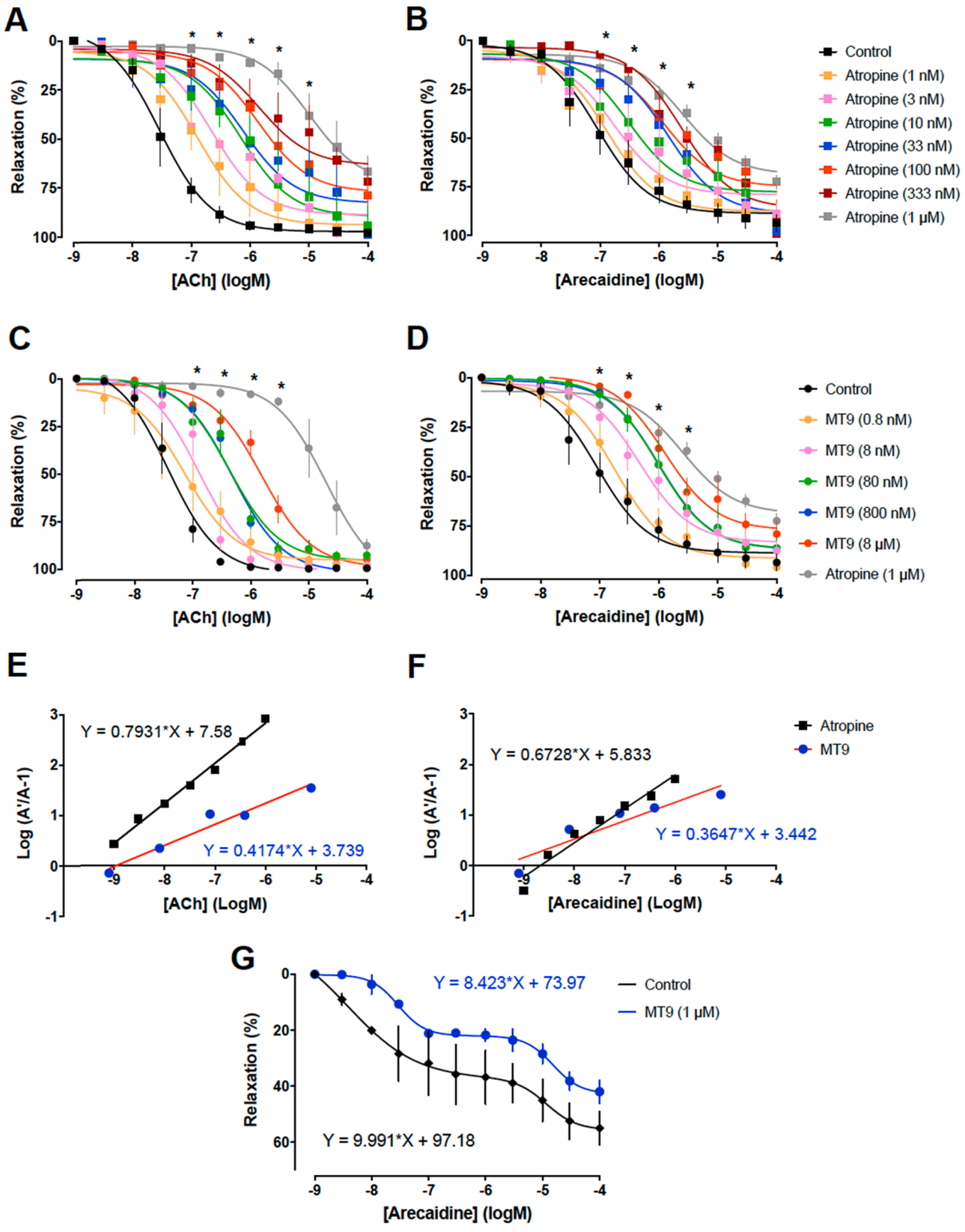

(caption on next page)

loop e2 of M2R, reinforces our hypothesis. Both MT9 and M2R show an unusual surface charge distribution that might be involved in their molecular interaction, probably associated with a new binding strategy that should be analyzed.

MT9 displays a high selectivity for M2R and induces an antagonist effect on the M2R/G_i pathway. On rat mesenteric arteries, MT9 can be

Fig. 7. Effects of MT9 on isolated rat and human arterial rings. (A) Concentration-response curves to ACh on isolated rat mesenteric arteries in the absence or presence of atropine at different concentrations. Atropine was incubated with arterial rings 30 min before challenging with ACh. Results are expressed as mean ± SEM (n = 5 artery preparations / condition and n = 2–4 arterial rings per data point for each preparation). * , $p < 0.05$, control *vs* all concentrations tested. (B) Concentration-response curves to arecaine on isolated rat mesenteric arteries in the absence or presence of atropine at different concentrations. Atropine was incubated with arterial rings 30 min before challenging with ACh. Results are expressed as mean ± SEM (n = as in A). *, $p < 0.05$, control *vs* all concentrations tested. (C) Concentration-response curves to ACh on isolated rat mesenteric arteries in the presence of MT9 at different concentrations or in the presence of 1 μM of atropine for comparison. MT9 was incubated with arterial rings 30 min before challenging with ACh. Results are expressed as mean ± SEM (n = as in A). *, $p < 0.05$, control *vs* all concentrations tested. (D) Concentration-response curves to arecaine on isolated rat mesenteric arteries in the presence of MT9 at different concentrations and 1 μM of atropine. Both atropine or MT9 were incubated with arterial rings 30 min before challenging with ACh. Results are expressed as mean ± SEM (n = 5/group). *, $p < 0.05$, control *vs* all concentrations tested. (E) Schild representation of MT9 and atropine effect with ACh. (F) Schild representation of MT9 and atropine effect with arecaine. (G) Concentration-response curves to arecaine on human internal mammary arteries rings in the absence or presence of 1 μM of MT9. Results are expressed as mean ± SEM (n = 2 human arterial preparations and n = 2–4/preparation).

Table 2
IC_{50} values of ACh- and arecaidine-induced rat mesenteric artery relaxation in the presence of variable atropine or MT9 concentrations.

	ACh		Arecaidine	
	IC_{50}	$LogIC_{50}$	IC_{50}	$LogIC_{50}$
Control	29.1 nM	-7.536 ± 0.085	89.7 nM	-7.047 ± 0.122
Atropine 1 nM	128 nM	-6.893 ± 0.146	127.3 nM	-6.895 ± 0.116
Atropine 3 nM	220.3 nM	-6.657 ± 0.095	173.7 nM	-6.760 ± 0.216
Atropine 10 nM	695.5 nM	-6.158 ± 0.191	309.0 nM	-6.510 ± 0.155
Atropine 33 nM	762.7 nM	-6.118 ± 0.206	1.19 μM	-5.924 ± 0.139
Atropine 100 nM	1.36 μM	-5.867 ± 0.128	1.449 μM	-5.839 ± 0.108
Atropine 333 nM	1.41 μM	-5.851 ± 0.213	2.42 μM	-5.617 ± 0.112
Atropine 1 μM	10.1 μM	-4.993 ± 0.163	2.57 μM	-5.591 ± 0.099
MT9 0.8 nM	73.71 nM	-7.132 ± 0.144	184.5 nM	-6.734 ± 0.102
MT9 8 nM	128.9 nM	-6.890 ± 0.081	471.8 nM	-6.326 ± 0.112
MT9 80 nM	424.0 nM	-6.373 ± 0.090	974.5 nM	-6.011 ± 0.111
MT9 800 nM	478.4 nM	-6.320 ± 0.048	1.02 μM	-5.990 ± 0.118
MT9 8 μM	1.55 μM	-5.810 ± 0.071	1.27 μM	-5.896 ± 0.110

envisioned as a full non-competitive antagonist whatever the agonist used, as their Schild representations have slopes much lower than the ones obtained with atropine. The fact that MT9 fully reverses acetylcholine and arecaidine relaxation suggests that the predominant role in relaxing pre-contracted mesenteric arteries is only mediated by the M2R. We also validated the MT9 antagonistic property on human internal mammary arteries. Interestingly, arecaidine interacts with high (low nM) and low affinity (low μM) on this preparation and MT9 selectively affects the high affinity sites. In this model, we suppose that the high affinity component is due to the activation of the M2R antagonized by MT9 and that the low affinity sites derives from other muscarinic subtypes, such as M1R already described in this arterial preparation [50]. These findings suggest a clear component of the M2R in human mammary artery and that MT9 is selective to this subtype. This is presumably not a major contribution according to the level of relaxation induced by arecaidine at low concentrations, which agrees with the study of Pesic [50]. In coherence with the physiological role of M2R, we would expect that MT9 induces an elevation in blood pressure and of the heart rate in vivo. Also, increases in the contractile force of the atrial cardiac muscle and of the conduction velocity of the atrioventricular node should occur, but all these effects need confirmation by adequate *in vivo* experiments.

Two other 3FTx have been described as M2R selective toxins, the natural M2-tox [24] and the artificial Tx24 generated by molecular engineering from the MT7 [4]. Interestingly, the 3D structure of the MT7-M1R complex has recently been solved [4], deciphering the molecular basis of the huge affinity and selectivity of this interaction. Unfortunately, it is not the case of the Tx24-M2R complex, precluding any structural explanation associated with the acquired M2 selectivity of this *in vitro*-engineered toxin. Furthermore, MT9 and Tx24 have very low sequence identity (26%, mainly due to the eight conserved cysteines: Fig. 5 A) and display different pharmacological properties (competitive antagonist for MT9 and allosteric modulator for Tx24), making it unlikely that these two M2R-selective toxins would interact similarly on this receptor subtype. Further studies are therefore required to understand the origin of the M2R selectivity of these toxins at the molecular level. Therefore, MT9 appears as a M2R-selective tool to decipher functions in arteries and investigating potential therapeutic opportunities in cardio-vascular diseases.

Funding

This work was supported by the French Agence Nationale de la Recherche grants for "venompicoscreen" and "Laboratory of Excellence Ion Channels, Science and Therapeutics" (ANR-11-LABX-0015). We also thank the Région Pays de la Loire (nouvelle équipe, 2016–11092/11093) and the European FEDER (2017/FEDER/PL0014592) for their support.

CRediT authorship contribution statement

JC, **JD**, **BL**, **CG**, **ES**, **PR**, **GB**, **MDW**, **NG**: Conceptualization. **JC**, **CZ**, **MB**, **CG**, **DB**, **LC**, **LT**, **MT**, **MF**: data collection. **MDW**, **NG**, **DS**, **RB**: Supervision. **JD**, **MT**, **BL**, **GM**, **CGE**: Methodology. PL, RB, IF: Resources. **JC**, **GM**, **BS**, **BL**, **CG**, **DS**, **NG**, **MDW**: Data analyses and interpretation. **GB**, **PR**, **CGE**, **RB**, **DS**, **NG**, **MDW**: Writing – Original draft. **MDW**: Critical revision of the manuscript.

Competing interest

CZ and **RB** are employees of Smartox Biotechnologies, while **MDW** is a founder and consultant of the company.

Declaration of Competing Interest

The authors declare the following financial interests/personal relationships which may be considered as potential competing interests: Michel De Waard reports equipment, drugs, or supplies was provided by Smartox Biotechnology. Michel De Waard reports a relationship with Smartox Biotechnology that includes: consulting or advisory.

Appendix A. Supporting information

Supplementary data associated with this article can be found in the online version at doi:10.1016/j.biopha.2022.113094.

References

[1] E.C. Hulme, N.J. Birdsall, N.J. Buckley, Muscarinic receptor subtypes, Annu Rev. Pharm. Toxicol. 30 (1990) 633–673.
[2] M.P. Caulfield, N.J. Birdsall, International union of pharmacology. XVII. Classification of muscarinic acetylcholine receptors, Pharm. Rev. 50 (2) (1998) 279–290.
[3] J. Wess, R.M. Eglen, D. Gautam, Muscarinic acetylcholine receptors: mutant mice provide new insights for drug development, Nat. Rev. Drug Discov. 6 (9) (2007) 721–733.
[4] S. Maeda, J. Xu, N.K. FM, M.J. Clark, J. Zhao, N. Tsutsumi, J. Aoki, R.K. Sunahara, A. Inoue, K.C. Garcia, B.K. Kobilka, Structure and selectivity engineering of the M1 muscarinic receptor toxin complex, Science 369 (6500) (2020) 161–167.

[5] K. Haga, A.C. Kruse, H. Asada, T. Yurugi-Kobayashi, M. Shiroishi, C. Zhang, W. I. Weis, T. Okada, B.K. Kobilka, T. Haga, T. Kobayashi, Structure of the human M2 muscarinic acetylcholine receptor bound to an antagonist, Nature 482 (7386) (2012) 547–551.

[6] A.C. Kruse, B.K. Kobilka, D. Gautam, P.M. Sexton, A. Christopoulos, J. Wess, Muscarinic acetylcholine receptors: novel opportunities for drug development, Nat. Rev. Drug Discov. 13 (7) (2014) 549–560.

[7] D.M. Thal, B. Sun, D. Feng, V. Nawaratne, K. Leach, C.C. Felder, M.G. Bures, D. A. Evans, W.I. Weis, P. Bachhawat, T.S. Kobilka, P.M. Sexton, B.K. Kobilka, A. Christopoulos, Crystal structures of the M1 and M4 muscarinic acetylcholine receptors, Nature 531 (7594) (2016) 335–340.

[8] P. Kovoor, K. Wickman, C.T. Maguire, W. Pu, J. Gehrmann, C.I. Berul, D. E. Clapham, Evaluation of the role of I(KACh) in atrial fibrillation using a mouse knockout model, J. Am. Coll. Cardiol. 37 (8) (2001) 2136–2143.

[9] R.D. Harvey, A.E. Belevych, Muscarinic regulation of cardiac ion channels, Br. J. Pharm. 139 (6) (2003) 1074–1084.

[10] L.M. Ren, T. Nakane, S. Chiba, Muscarinic receptor subtypes mediating vasodilation and vasoconstriction in isolated, perfused simian coronary arteries, J. Cardiovasc. Pharm. 22 (6) (1993) 841–846.

[11] M. Niihashi, M. Esumi, Y. Kusumi, Y. Sato, I. Sakurai, Expression of muscarinic receptor genes in the human coronary artery, Angiology 51 (4) (2000) 295–300.

[12] C.B. Treasure, S.V. Manoukian, J.L. Klein, J.A. Vita, E.G. Nabel, G.H. Renwick, A. P. Selwyn, R.W. Alexander, P. Ganz, Epicardial coronary artery responses to acetylcholine are impaired in hypertensive patients, Circ. Res. 71 (4) (1992) 776–781.

[13] M.G. Hendriks, M. Pfaffendorf, P.A. Van Zwieten, Characterization of the muscarinic receptor subtype mediating vasodilation in the rat perfused mesenteric vascular bed preparation, J. Auton. Pharm. 12 (6) (1992) 411–420.

[14] P. Tangsucharit, S. Takatori, Y. Zamami, M. Goda, P. Pakdeechote, H. Kawasaki, F. Takayama, Muscarinic acetylcholine receptor M1 and M3 subtypes mediate acetylcholine-induced endothelium-independent vasodilatation in rat mesenteric arteries, J. Pharm. Sci. 130 (1) (2016) 24–32.

[15] J.K. Phillips, M. Vidovic, C.E. Hill, Variation in mRNA expression of alpha-adrenergic, neurokinin and muscarinic receptors amongst four arteries of the rat, J. Auton. Nerv. Syst. 62 (1–2) (1997) 85–93.

[16] R. Hammer, E. Giraldo, G.B. Schiavi, E. Monferini, H. Ladinsky, Binding profile of a novel cardioselective muscarine receptor antagonist, AF-DX 116, to membranes of peripheral tissues and brain in the rat, Life Sci. 38 (18) (1986) 1653–1662.

[17] F. Dorje, J. Wess, G. Lambrecht, R. Tacke, E. Mutschler, M.R. Brann, Antagonist binding profiles of five cloned human muscarinic receptor subtypes, J. Pharm. Exp. Ther. 256 (2) (1991) 727–733.

[18] O. Pfaff, C. Hildebrandt, M. Waelbroeck, X. Hou, U. Moser, E. Mutschler, G. Lambrecht, The (S)-(+)-enantiomer of dimethindene: a novel M2-selective muscarinic receptor antagonist, Eur. J. Pharm. 286 (3) (1995) 229–240.

[19] E. Karlsson, M. Jolkkonen, E. Mulugeta, P. Onali, A. Adem, Snake toxins with high selectivity for subtypes of muscarinic acetylcholine receptors, Biochimie 82 (9–10) (2000) 793–806.

[20] D. Servent, C. Fruchart-Gaillard, Muscarinic toxins: tools for the study of the pharmacological and functional properties of muscarinic receptors, J. Neurochem. 109 (5) (2009) 1193–1202.

[21] D. Servent, G. Blanchet, G. Mourier, C. Marquer, E. Marcon, C. Fruchart-Gaillard, Muscarinic toxins, Toxicon 58 (6–7) (2011) 455–463.

[22] C. Fruchart-Gaillard, G. Mourier, C. Marquer, E. Stura, N.J. Birdsall, D. Servent, Different interactions between MT7 toxin and the human muscarinic M1 receptor in its free and N-methylscopolamine-occupied states, Mol. Pharm. 74 (6) (2008) 1554–1563.

[23] C. Marquer, C. Fruchart-Gaillard, G. Letellier, E. Marcon, G. Mourier, S. Zinn-Justin, A. Menez, D. Servent, B. Gilquin, Structural model of ligand-G protein-coupled receptor (GPCR) complex based on experimental double mutant cycle data: MT7 snake toxin bound to dimeric hM1 muscarinic receptor, J. Biol. Chem. 286 (36) (2011) 31661–31675.

[24] J.M. Carsi, H.H. Valentine, L.T. Potter, m2-toxin: A selective ligand for M2 muscarinic receptors, Mol. Pharm. 56 (5) (1999) 933–937.

[25] J. Ciolek, H. Reinfrank, L. Quinton, S. Viengchareun, E.A. Stura, L. Vera, S. Sigismeau, B. Mouillac, H. Orcel, S. Peigneur, J. Tytgat, L. Droctove, F. Beau, J. Nevoux, M. Lombes, G. Mourier, E. De Pauw, D. Servent, C. Mendre, R. Witzgall, N. Gilles, Green mamba peptide targets type-2 vasopressin receptor against polycystic kidney disease, Proc. Natl. Acad. Sci. USA 114 (27) (2017) 7154–7159.

[26] G.M. Fang, Y.M. Li, F. Shen, Y.C. Huang, J.B. Li, Y. Lin, H.K. Cui, L. Liu, Protein chemical synthesis by ligation of peptide hydrazides, Angew. Chem. Int Ed. Engl. 50 (33) (2011) 7645–7649.

[27] G. Blanchet, D. Alili, A. Protte, G. Upert, N. Gilles, L. Tepshi, E.A. Stura, G. Mourier, D. Servent, Ancestral protein resurrection and engineering opportunities of the mamba aminergic toxins, Sci. Rep. 7 (1) (2017) 2701.

[28] L. Ciccone, L. Vera, L. Tepshi, L. Rosalia, A. Rossello, E.A. Stura, Multicomponent mixtures for cryoprotection and ligand solubilization, Biotechnol. Rep. 7 (2015) 120–127.

[29] I. Polsinelli, M. Savko, C. Rouanet-Mehouas, L. Ciccone, S. Nencetti, E. Orlandini, E.A. Stura, W. Shepard, Comparison of helical scan and standard rotation methods in single-crystal X-ray data collection strategies, J. Synchrotron Radiat. 24 (Pt 1) (2017) 42–52.

[30] W. Kabsch, Integration, scaling, space-group assignment and post-refinement, Acta Crystallogr D. Biol. Crystallogr 66 (Pt 2) (2010) 133–144.

[31] P. Legrand, Xdsme: Xds made easier, (2010), https://github.com/legrandp/xdsme.

[32] X. Lou, X. Tu, G. Pan, C. Xu, R. Fan, W. Lu, W. Deng, P. Rao, M. Teng, L. Niu, Purification, N-terminal sequencing, crystallization and preliminary structural determination of atratoxin-b, a short-chain alpha-neurotoxin from Naja atra venom, Acta Crystallogr. D. Biol. Crystallogr. 59 (Pt 6) (2003) 1038–1042.

[33] A.J. McCoy, R.W. Grosse-Kunstleve, P.D. Adams, M.D. Winn, L.C. Storoni, R. J. Read, Phaser crystallographic software, J. Appl. Crystallogr. 40 (Pt 4) (2007) 658–674.

[34] G.N. Murshudov, P. Skubak, A.A. Lebedev, N.S. Pannu, R.A. Steiner, R.A. Nicholls, M.D. Winn, F. Long, A.A. Vagin, REFMAC5 for the refinement of macromolecular crystal structures, Acta Crystallogr. D. Biol. Crystallogr. 67 (Pt 4) (2011) 355–367.

[35] P.D. Adams, P.V. Afonine, G. Bunkoczi, V.B. Chen, I.W. Davis, N. Echols, J. J. Headd, L.W. Hung, G.J. Kapral, R.W. Grosse-Kunstleve, A.J. McCoy, N. W. Moriarty, R. Oeffner, R.J. Read, D.C. Richardson, J.S. Richardson, T. C. Terwilliger, P.H. Zwart, PHENIX: a comprehensive Python-based system for macromolecular structure solution, in: Acta Crystallogr. D Biol Crystallogr., 66, 2010, pp. 213–221.

[36] P. Emsley, B. Lohkamp, W.G. Scott, K. Cowtan, Features and development of Coot, Acta Crystallogr. D. Biol. Crystallogr. 66 (Pt 4) (2010) 486–501.

[37] W.L. DeLano, The PyMOL Molecular Graphics System, in: L. Schrödinger (Ed.), New York, 2010.

[38] S. Unni, Y. Huang, R.M. Hanson, M. Tobias, S. Krishnan, W.W. Li, J.E. Nielsen, N. A. Baker, Web servers and services for electrostatics calculations with APBS and PDB2PQR, J. Comput. Chem. 32 (7) (2011) 1488–1491.

[39] G. Blanchet, G. Collet, G. Mourier, N. Gilles, C. Fruchart-Gaillard, E. Marcon, D. Servent, Polypharmacology profiles and phylogenetic analysis of three-finger toxins from mamba venom: case of aminergic toxins, Biochimie 103 (2014) 109–117.

[40] K. Tamura, G. Stecher, D. Peterson, A. Filipski, S. Kumar, MEGA6: molecular evolutionary genetics analysis version 6.0, Mol. Biol. Evol. 30 (12) (2013) 2725–2729.

[41] G. Mourier, S. Dutertre, C. Fruchart-Gaillard, A. Menez, D. Servent, Chemical synthesis of MT1 and MT7 muscarinic toxins: critical role of Arg-34 in their interaction with M1 muscarinic receptor, Mol. Pharm. 63 (1) (2003) 26–35.

[42] Y. Cheng, W.H. Prusoff, Relationship between the inhibition constant (K1) and the concentration of inhibitor which causes 50 per cent inhibition (I50) of an enzymatic reaction, Biochem. Pharm. 22 (23) (1973) 3099–3108.

[43] A. Adem, E. Karlsson, Muscarinic receptor subtype selective toxins, Life Sci. 60 (13–14) (1997) 1069–1076.

[44] F.J. Joubert, N. Taljaard, The complete primary structures of two reduced and S-carboxymethylated Angusticeps-type toxins from Dendroaspis angusticeps (green mamba) venom, Biochim. Biophys. Acta 623 (2) (1980) 449–456.

[45] J.M. Conlon, M. Prajeep, M. Mechkarska, K. Arafat, S. Attoub, A. Adem, D. Pla, J. J. Calvete, Peptides with in vitro anti-tumor activity from the venom of the Eastern green mamba, Dendroaspis angusticeps (Elapidae), J. Venom. Res. 5 (2014) 16–21.

[46] J.R. de Weille, H. Schweitz, P. Maes, A. Tartar, M. Lazdunski, Calciseptine, a peptide isolated from black mamba venom, is a specific blocker of the L-type calcium channel, Proc. Natl. Acad. Sci. USA 88 (6) (1991) 2437–2440.

[47] Y. Bourne, P. Taylor, P. Marchot, Acetylcholinesterase inhibition by fasciculin: crystal structure of the complex, Cell 83 (3) (1995) 503–512.

[48] B.G. Fry, W. Wuster, R.M. Kini, V. Brusic, A. Khan, D. Venkataraman, A.P. Rooney, Molecular evolution and phylogeny of elapid snake venom three-finger toxins, J. Mol. Evol. 57 (1) (2003) 110–129.

[49] U. Moser, G. Lambrecht, M. Wagner, J. Wess, E. Mutschler, Structure-activity relationships of new analogues of arecaidine propargyl ester at muscarinic M1 and M2 receptor subtypes, Br. J. Pharm. 96 (2) (1989) 319–324.

[50] S. Pesic, A. Jovanovic, L. Grbovic, Muscarinic receptor subtypes mediating vasorelaxation of the perforating branch of the human internal mammary artery, Pharmacology 63 (3) (2001) 185–190.

[51] V. Tsetlin, Snake venom alpha-neurotoxins and other 'three-finger' proteins, Eur. J. Biochem. 264 (2) (1999) 281–286.

[52] P. Kessler, P. Marchot, M. Silva, D. Servent, The three-finger toxin fold: a multifunctional structural scaffold able to modulate cholinergic functions, J. Neurochem. 142 (Suppl 2) (2017) 7–18.

[53] C.C. Chang, C.Y. Lee, Isolation of neurotoxins from the venom of Bungarus multitinctus and their modes of neuromuscular blocking action, Arch. Int. Pharm. 144 (1963) 241–257.

[54] J.P. Changeux, M. Kasai, C.Y. Lee, Use of a snake venom toxin to characterize the cholinergic receptor protein, Proc. Natl. Acad. Sci. USA 67 (3) (1970) 1241–1247.

[55] A. Maiga, G. Mourier, L. Quinton, C. Rouget, C. Gales, C. Denis, P. Lluel, J. M. Senard, S. Palea, D. Servent, N. Gilles, G protein-coupled receptors, an unexploited animal toxin targets: Exploration of green mamba venom for novel drug candidates active against adrenoceptors, Toxicon 59 (4) (2012) 487–496.